GaN-based High Frequency High Power Density 2-in-1 Bidirectional OBCM Design for EV Application

Minli Jia[1], Hao Sun[1]

[1] Navitas Semiconductor Shanghai EV Design Center, China

Corresponding author: Jia Minli, minli.jia@navitassemi.com

Abstract

The product design based on GaN devices can improve the switching frequency, reduce the volume of passive devices, and further optimize the product power density and cost. However, due to the small die size and fast switching characteristics of GaN devices, it brings a series of new challenges to heat dissipation design, drive design and magnetic component design. Based on the integrated "2-in-1" design of bidirectional 6.6kw OBC and 3.0kW LV-DC/DC, this paper proposes an efficient heat dissipation technology using Navitas integrated drive GaN-Power-IC devices. The switching frequency of CCM-PFC is set as 100khz, and the switching frequency of soft switch Bidirectional Boost-SRC is above 400khz, and the maximum operating frequency is 800khz. The volume of PFC inductance and transformer are reduced significantly, power density up to 3.9kW/L.

1 Introduction

Bidirectional OBC and LV-DC/DC are the two main energy conversion units of EV. Physical integration and magnetic integration are two common methods to improve power density. The magnetic integration method is limited by the coupling between the ports and must be decoupled [1-2]. However, physical integration can be flexible and free control, which is widely used in product design.

Full-bridge PFC and Totem-pole PFC [3] are two main bidirectional AC/DC topologies, both of which can realize frequency doubling of AC side ripple current. However, full-bridge PFC topology has serious common-mode noise, which brings challenges to EMI design. Totem-pole PFC adopts the control mode of fast and slow bridge arms matching to overcome the problem of common mode noise. In addition, totem-pole PFC usually adopt interleaving architecture to achieve efficiency and cost optimization.

DAB and CLLC are the two main topologies of bidirectional DC/DC. DAB [4] is limited by its small soft switching range and is not suitable for the application of wide voltage range output. CLLC [5-7] can realize switches full range of ZVS turn-on, but its Bus voltage needs to be adjusted in a wide range, which will increase the cost of Bus capacitance. Therefore, literature [8-9] proposes a delay-time control strategy to achieve the output voltage gain regulation, ZVS switching and without wide range of bus voltage regulation, which is very suitable for the application of vehicle charging.

As another energy conversion unit in EV, LV-DC/DC converts the voltage of the high-voltage battery to 12V to charge the low-voltage battery, and at the same time supplies power to the internal lighting, audio, video entertainment and automatic driving system, etc. Due to its wide voltage range of input and output, it is difficult for the traditional LLC design to match the full-range output voltage. Therefore, the hard switching full-bridge with center-tap controlled by PWM is the preferred topology and widely used.

GaN device is attracting the attention of the industry because of its characteristics of high switching frequency, low resistance and zero reverse recovery charge [10]. However, the crosstalk between bridge arms caused by fast switching increases the risk of shoot-through, which puts forward higher requirements for the drive design [11]. The 650V enhanced GaN device adopts the normally closed gate transistor structure, and its internal integrated drive disturbance rejection unit improves the reliability of the device and ensures the safe and efficient operation of the power electronic device. In addition, the die size of GaN is 1/5 that of Si and 2/3 that of SiC for the same conduction capacity[12], as shown in Fig. 1. The heat dissipation design of GaN has higher requirements, so reliable heat dissipation design must be carried out.

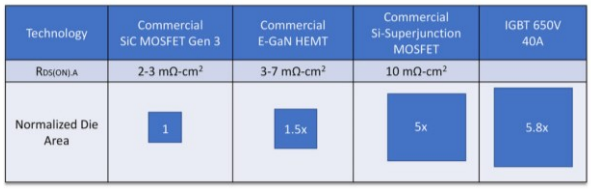

Fig. 1 Die size comparison of Si, SiC and GaN

The system topology shown in Fig. 2, interleaved totem-pole PFC for AC/DC stage, whereD1 and D2 are to prevent the action of surge current. Bidirectional ZVS Boost-SRC for DC/DC stage. Hard switching center-tap full-bridge topology for HV to LV stage. The switches (Q1~Q4, S1~S12) are all designed with GaN devices.

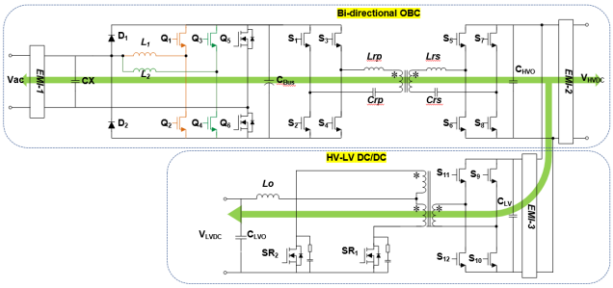

Fig. 2 System topology

2 Bi-AC/DC Stage

DCM, TCM, and CCM are the three control modes of totem-pole PFC. Where DCM and TCM control mode can realize the switching ZVS, high frequency and small inductance, which is suitable for only rectifier transformation requirement. CCM control mode has continuous inductance current and need large inductance value, which is a general control method of bidirectional application，its disadvantage is that the switching loss is large, and the switching frequency limited by using traditional Si devices. Compared with Si devices, the switching frequency of GaN can be operated above 100khz, and the volume of inductance can be further reduced.

2.1 AC/DC Inductance Design

The inductance calculation in CCM mode has been introduced in many documents. The optimal inductance design is the result of trade-off consideration based on device switching loss, EMI and THD of the system. According to the working characteristics of totem-pole PFC, when the input voltage Vac is equal to half of the voltage of Vbus, the ripple current of inductance is maximum. The formula for calculating the minimum inductance is as follows:

$$L_{PFC\_\min} = \frac{V_{Bus}/2}{k_{Ripple} \cdot \sqrt{2} \cdot I_{Ac\_rms} \cdot 2 \cdot f_s} \qquad (1)$$

Where, f_s is the switching frequency, k_{Ripple} is the ripple coefficient and I_{Ac_rms} is the RMS value of the input. Usually, the total value of k_{Ripple} is required to be less than 0.5, so its value for single channel PFC can be less than 1. Based on the design parameters in Table 1, it can be obtained that the minimum inductance satisfying the demand is 45uH according to formula (1).

Single-phase PFC inductor design	
Electronic Parameters	Value
Vac	220V
Iac_RMS	16A
Vbus	400V
f_Linef_s	50hz/100khz

Table 1 Single channel main parameters

The expression of duty ratio D of unipolar modulation is as follows：

$$D(t) = 1 - \frac{\sqrt{2}\,Vac\,|\sin(2\pi f_{line} t)|}{Vbus} \qquad (2)$$

The current ripple in the switching period is:

$$\Delta i(t) = \frac{\sqrt{2}\,Vac\,|\sin(2\pi f_{line} t)|}{L_{PFC\_\min}} D(t) \frac{1}{f_s} \qquad (3)$$

The average current is：

$$i_{avg}(t) = \sqrt{2}\, I_{Ac\_rms} |\sin(2\pi f_{line} t)| \qquad (4)$$

According to equations (3) and (4), the waveforms of current ripple and average value change in half a cycle are obtained, as shown in Fig. 3.

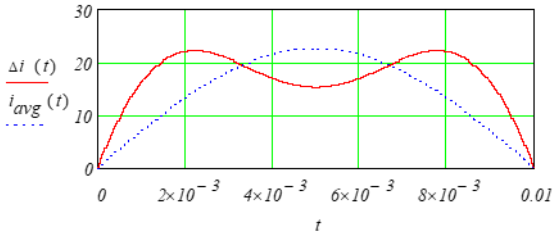

Fig. 3 Average and ripple Current of inductor

2.2 Magnetic material selection

Ferrite and metal magnetic core are two common types of magnetic materials. The advantage of ferrite soft magnetic is that it has high permeability and resistivity at high frequency, but its B value is much lower than the metal magnetic, and its anti-DC saturation ability is weak, which is suitable for using in high frequency transformers design. Technically, metal magnetic core can only make inductors, and the difference between it and ferrite is as follows:

(1) Metallic magnetic core B value is high, low permeability, can withstand greater DC bias.

(2) Metal magnetic core evenly distributes the air gap, small air gap loss.

(3) Metal magnetic cores have a wider operating temperature range than ferrites.

(4) Metal magnetic core inductor design is simple, don't need to test the dynamic indicators to verify the design.

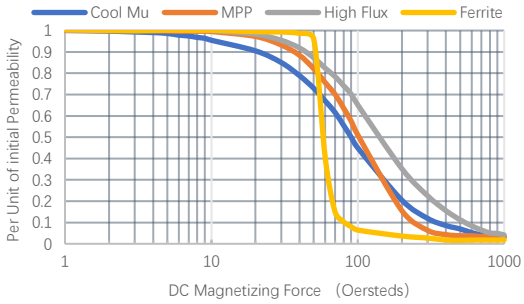

Fig. 4 Different magnetic materials comparison

Cool Mu, High-flux and MPP are common metallic magnetic cores, among which MPP has advantages of the highest relative permeability, the lowest core loss and the best high temperature characteristics, but disadvantage is that it contains 80% Ni and costs high. Cool Mu material has the highest core loss and the lowest cost. Fig. 4 shows the comparison of different magnetic materials with relative permeability of 60. It can be seen that with the increase of DC bias, High-flux has the best stability, while ferrite core has the worst.

Ring-shaped magnetic core is usually used in engineering design because of its uniform distribution of magnetic field. The initial inductance is calculated as follows:

$$L = \frac{0.4\pi \cdot u \cdot N^2 \cdot A_e}{l_e \cdot 10^3} \tag{5}$$

Where, $u = u_i \cdot u_0$ is the initial permeability, u_i is the relative permeability, N is the number of turns, A_e (mm^2)is the cross-sectional area, and l_e (mm)is the length of the magnetic circuit. When DC bias exists, the magnetic field intensity at the peak AC current is H and calculated by expression (6). The coefficient k of relative permeability can be got from the ordinate (Fig. 4), and the inductance after magnetic bias considered can be obtained as: $L_1 = K \cdot L$.

$$H = \frac{N \cdot I}{l_e \cdot 10^{-1}} \tag{6}$$

When the PFC stage switching frequency changes from 50khz to 100khz, the inductance volume decreases by about 200%, as shown in Fig.5.

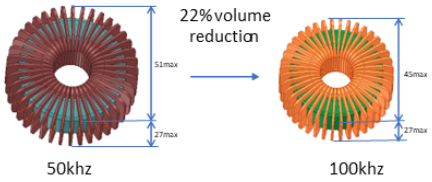

Fig. 5 Inductor size comparison

3 Bi-DC/DC Stage

The CLLC control strategy is divided into two categories, one is LLC-like Vary-frequency control, and another is combining Vary-frequency and phase shift control. The main difference between the two applications is that the LLC-like control method requires the wide bus voltage, so as to achieve the optimal gain and efficiency, which is widely used in the conduction with three-phase AC input. The method of Vary-switching frequency plus phase-shift (delay-time) control can realize the output of high gain and wide voltage even under the constant bus voltage conduction, so this control strategy is also called Boost-SRC, which is very suitable for single-phase OBC application. The literature [8-9] has detailed analysis about the delay-time control, and this paper only gives a brief introduction.

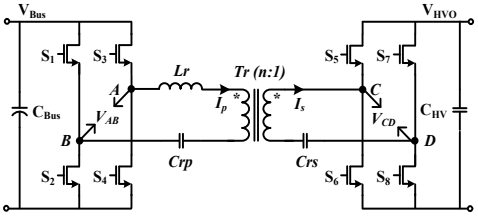

Fig. 6 Topology of bidirectional DC/DC

Fig. 6 shows the bidirectional DC/DC topology. S_1~S_8 are the switching devices, the transformer turn ratio is $n = Np/Ns$, the resonant capacitance meets: $Crp = 2 \cdot Cr$, $Crs = 2 \cdot Cr \cdot n^2$, and the equivalent resonant capacitance and inductor are respectively Cr and L_r, V_{AB} and V_{CD} are the midpoint voltage of Bus and battery side bridge

arm respectively. The resonant frequency is defined as:

$$f_r = \frac{1}{2 \cdot \pi \cdot \sqrt{L_r \cdot C_r}} \tag{7}$$

3.1 Working Mode Analysis

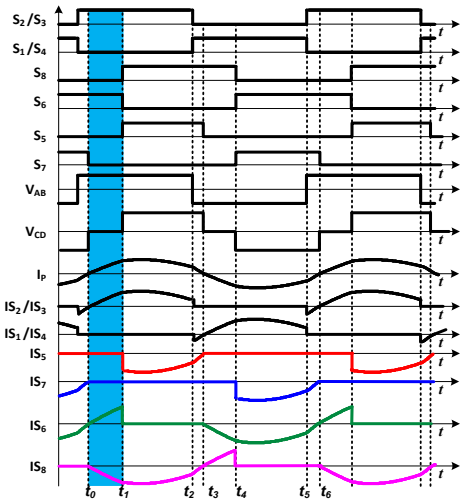

Fig. 7 Control strategy and key waveforms

For the bidirectional resonant Boost-SRC, when the gain is less than 1, Vary-frequency modulation control is used, which will not be detailed. When the gain is greater than 1, phase-shift control is used to improve the gain. Fig. 7 shows the typical waveforms of bidirectional Boost-SRC at the gain greater than 1. Simplicity, the dead time is ignored. Detailed state analysis only for half a cycle.

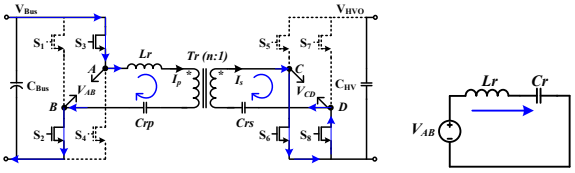

Fig. 8 Mode 1 switching state and equivalent circuit

Working mode 1 [t_0, t_1]: at t_0, S_2/S_3 is turned on, the resonant current changes from negative to positive, the primary side V_{Bus} excites the resonant tank; the secondary side resonant current shorts through the switches S_6 and S_8. The resonant inductor enters the energy storage stage and like a boost inductance. The equivalent circuit is shown in Fig. 8. According to KVL's law, the equation is as follows:

$$L_r \frac{\mathrm{d}i_{Lr}}{\mathrm{d}t} + u_{Cr} = V_{AB} \tag{8}$$

Also $C_r\, du_{Cr}/dt = i_{Lr}$, formula (8) can be expressed as:

$$L_r C_r \frac{\mathrm{d}^2 u_{Cr}}{\mathrm{d}t^2} + u_{Cr} = V_{AB} \tag{9}$$

The initial state is defined as: $u_{Cr}(t_0) = u_{Cr0}$, $i_{Lr}(t_0) = 0$, $\omega_r = 1/\sqrt{L_r C_r}$, and the differential solution of formula (8) and (9) can be obtained:

$$u_{Cr1}(t) = (u_{Cr0} - V_{AB})\cos(\omega_r t) + V_{AB} \tag{10}$$

$$i_{Lr1}(t) = \sqrt{\frac{C_r}{L_r}}(u_{Cr0} - V_{AB})\sin(\omega_r t) \tag{11}$$

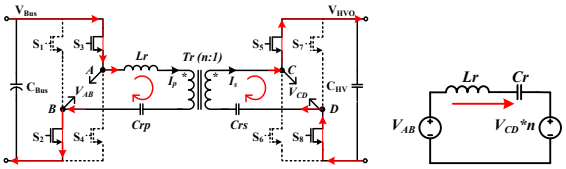

Fig. 9 Mode 2 switching state and equivalent circuit

Working mode 2 [t_1, t_2]: at t_1, S_6 turn-off and S_8 ZVS turn-on. On the one hand，the resonant tank receives energy from V_{Bus} and on the other hand transfers energy to the output. The equivalent circuit is shown in Fig. 9.

The expressions of resonant capacitance and current at this stage are as follows：

$$u_{Cr2}(t) = (u_{Cr1}(t_1) - V_{AB} + nV_{CD})\cos(\omega_r t) + V_{AB} - nV_{CD} \tag{12}$$

$$i_{Lr2}(t) = \sqrt{\frac{C_r}{L_r}}(u_{Cr1}(t_1) - V_{AB} + nV_{CD})\sin(\omega_r t) \tag{13}$$

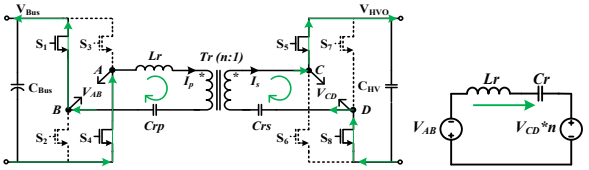

Fig. 10 Mode 3 switching state and equivalent circuit

Working mode 3 [t_2, t_3]: At t_2, S_2/S_3 turn-off and S_1/S_4 ZVS turn-on. The energy in the resonant tank feeds energy to the primary side and at the same time transfers energy to the output. The equivalent circuit is shown in Fig.10.

At t_2, the primary side current is commutated. To realize S_1/S_4 ZVS turn-on, the resonant current at this moment should be large enough to meet the

demand of charging the capacitance Coss of the switches. The energy relation can be as follows:

$$L_{r\_ZVS} \cdot i_{Lr}(t_2)^2 > 2Coss \cdot V_{Bus}^2 \quad (14)$$

The minimum current satisfying the switch ZVS is:

$$i_{Lr\_ZVS\_Min} = V_{Bus} \cdot \sqrt{2\frac{Coss}{Lr}} \quad (15)$$

When the C_{oss} capacitance value is known, L_{r_ZVS} should be as small as possible to reduce reactive power loss. The expression of capacitor voltage and inductor current in this mode is as follows:

$$u_{Cr3}(t) = (u_{Cr2}(t_2) + V_{AB} + nV_{CD})\cos(\omega_r t) - V_{AB} - nV_{CD} \quad (16)$$

$$i_{Lr3}(t) = \sqrt{\frac{C_r}{L_r}}(u_{Cr2}(t_2) + V_{AB} + n \cdot V_{CD})\sin(\omega_r t) \quad (17)$$

To sum up, there are three working modes in half a switching cycle. Mode 1 is the core of the circuit to achieve gain increase, while mode 2 is a normal power transmission. Mode 3 is the energy feedback stage, providing ZVS working conditions.

3.2 Phase Plane Analysis

The idea of Phase plane analysis is to draw trajectories related to initial conditions on the phase plane, and then analyze the characteristics of these trajectories. LC resonant circuit as a second order system is suitable for phase plane analysis.

The characteristic impedance of the resonant tank is defined as: $R_0 = \sqrt{L_r/C_r}$, and all parameters are normalized based on V_{Bus} as follows:

- Input voltage: $M_{in} = V_{Bus}/V_{Bus} = 1$
- Output voltage: $M_o = n \cdot V_{HVO}/V_{Bus}$
- Peak voltage of C_r: $M_{CrP} = V_{Cr\_Pek}/V_{Bus}$
- Resonant capacitor voltage: $m_{Cr} = V_{Cr}/V_{Bus}$
- Resonant current: $j_{Lr} = R_0 \cdot i_{Lr}/V_{Bus}$
- Min. ZVS current: $h_1 = i_{Lr\_ZVS\_Min} \cdot R_0/V_{Bus}$

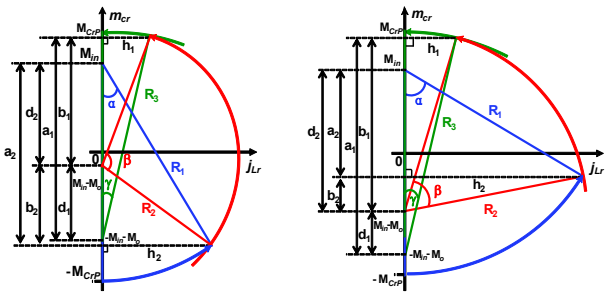

(a) a2> d2 (b) a2< d2

Fig. 11 Phase plane analysis of half switching cycle

The phase plane with gain >1 is shown in Fig. 11, which is divided into two cases according to the different sizes of a_2 and d_2. Take a_2>d_2 as an example, d_1=2M_{in}, d_2=M_o, R_1=M_{CrP}+M_{in}, R_3=M_{CRP}+M_o+M_{in}, and the following expression can be obtained according to the geometric relationship:

$$\begin{cases} a_1 - b_1 = d_1 \\ a_1^2 + h_1^2 = R_3^2 \\ b_1^2 + h_1^2 = R_2^2 \\ a_2 - b_2 = d_2 \\ a_2^2 + h_2^2 = R_1^2 \\ b_2^2 + h_2^2 = R_2^2 \end{cases} \quad (18)$$

From (18), a_1,h_1, a_2 and h_2 can be got:

$$a_1 = \frac{R_3^2 - R_2^2 + d_1^2}{2d_1} \quad (19)$$

$$h_1 = \sqrt{R_2^2 - a_1^2} \quad (20)$$

$$a_2 = \frac{R_1^2 - R_2^2 + d_2^2}{2d_2} \quad (21)$$

$$h_2 = \sqrt{R_1^2 - a_2^2} \quad (22)$$

Angle γ and α can be calculated as follows:

$$\gamma = \sin^{-1}\frac{h_1}{R_3} \quad (23)$$

$$\alpha = \sin^{-1}\frac{h_2}{R_1} \quad (24)$$

For half a switching cycle, α, β and γ angles meet:

$$\beta = \pi - \sin^{-1}\frac{h_1}{R_3} - \sin^{-1}\frac{h_2}{R_1} \quad (25)$$

So far, the expression of half cycle of resonant inductor current when gain >1 is:

$$i_{Lr}(t) = \begin{cases} \frac{V_{in}}{R_o}R_1\sin(\omega_r t) & 0 \le t < T_\alpha \\ \frac{V_{in}}{R_o}R_2\sin[\omega_r(t - T_\alpha) + \beta_{start\_angle}] & T_\alpha \le t < T_\alpha + T_\beta \\ \frac{V_{in}}{R_o}R_3\sin[\omega_r(t - T_\alpha - T_\beta) + \pi - \gamma] & T_\alpha + T_\beta \le t < \frac{T_s}{2} \end{cases} \quad (26)$$

Where, $\beta_{start\_angle} = \sin^{-1}(h_2/R_2)$, when α Angle is large, the working condition as shown in Fig.11 (b) will occur, and the initial Angle will become to $\beta_{start\_angle} = \pi - \sin^{-1}(h_2/R_2)$. It can be seen from

Fig. 11 that, as the α Angle increases, the turn-off current of the secondary side with phase-shift leg devices increases and reaches the maximum value when $\alpha = \pi/2$. When designed, the α Angle should be as small as possible, so as to ensure the optimal efficiency.

3.3 Boost SRC Characteristics Analysis

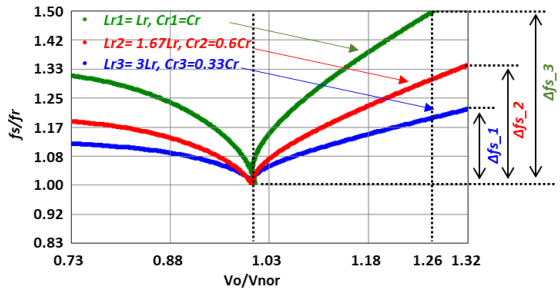

Fig. 12 Switching frequency range comparison

As an LC resonant circuit, Boost-SRC is simple in design because it does not require excitation inductance. Fig. 12 shows the influence of different resonant parameters on switching frequency range when keeping the same resonant frequency. The larger the inductance, the smaller Δfs of switching frequency variation. In resonant circuit, the capacitor voltage and inductive current of half a switching cycle complete an energy exchange, satisfying the following formula:

$$C_r \cdot V_{Cr\_Pek} = i_{lr\_avg} \cdot T_s/2 \qquad (27)$$

Where, i_{lr_avg} is the average value of resonant current in half a period. Under the condition of a constant output power, the value on the right side of equation (27) remains constant. When the inductance L_r increases, C_r will become smaller and V_{Cr_Pek} become larger. The selection of inductance and capacitance voltage tolerance in practical applications should be considered as a trade-off.

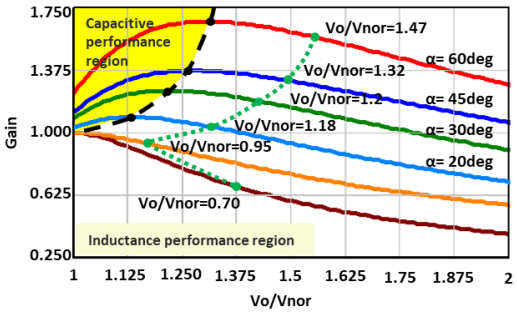

Fig. 13 Boost SRC gain curve

The gain expression of Boost SRC is described in detail in literature [8]. The gain curves of different angles α are shown in Fig. 13. Each curve corresponds to a different output voltage, and with the increase of phase-shift α Angle, the gain is constantly raised. Connect the peak points of each curve. The capacitive and inductance areas are distributed on its both sides. The design should ensure that it is in the inductance area to meet the ZVS action of the devices. When connecting the working points of each curve is its corresponding frequency change curve, and the existence of "V" shape can be seen.

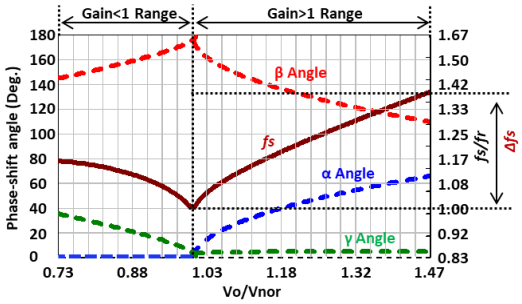

Fig. 14 α, β, γ and f_s vs Vo

Under constant output power, the variation curves of angles α, β, γ and f_s with the output voltage are shown in Fig. 14. When the gain is less than 1, the Angle of α is zero, and the Boost-SRC works in the over-resonant state, only vary-frequency control is carried out. In the area of gain greater than 1, with the increase of output voltage, the gain becomes larger, the Angle α increases, and the switching frequency increases accordingly. In the entire output voltage range, the switching frequency is greater than the resonant frequency, showing a "V" shape transformation, which is different from the traditional LLC "S" type switching frequency change, with a relatively narrow switching frequency change, which is conducive to the design of magnetic elements.

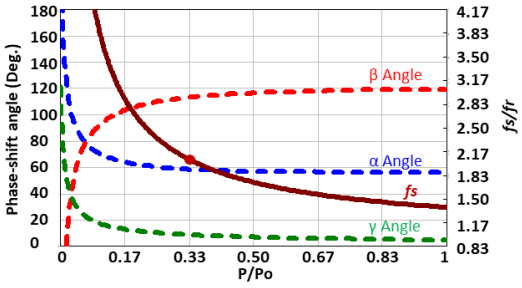

Fig. 15 α, β, γ and f_s vs Po

Under constant output voltage, the curve of Angle α, β, γ and f_s changing with the output power is shown in Fig.15. In the range of 30%~100% load, Angle α and f_s change little; When the load is below 30%, the Angle α will increase the

switching frequency rapidly and the system will enter “Burst” mode, which is a common phenomenon in frequency modulation.

3.4 Comparison of control strategy

The control of bidirectional Boost-SRC is flexible. The output gain can be regulated by arbitrarily selecting the two switches adjacent of the secondary side S_5~S_8 as phase shift control and the other two as synchronous rectifier control. However, the loss of the secondary side devices is different with different control strategies.

In the control strategy introduced in Fig. 6 above, S_6 and S_8 are secondary side phase shift switches, and S_5 and S_7 are synchronous rectifier switches. The advantage is that the phase-shift switches are all down devices, which is easy to drive circuit design. The disadvantage is that the phase-shift devices have large RMS current and turn-off loss. Fig. 16 (a) shows an optimized modulation strategy: S_7 and S_8 are the secondary side phase-shift devices, S_5 and S_6 are the synchronous rectification devices, the RMS current of the phase-shift devices is greatly reduced, and the conduction loss is reduced.

In order to achieve uniform loss of the four devices on the secondary side, another optimized control strategy is presented in Fig. 16 (b) : the four devices on the secondary side carry out phase-shift control in turn. It can be seen from the current waveform of S_6~S_8 that the conduction loss and turn-off loss are evenly distributed on the four devices, thus achieving the thermal balance of them.

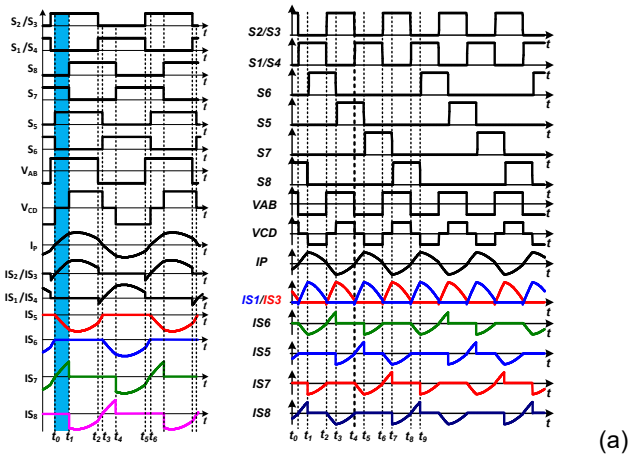

(a) Control strategy 1 (b) Control strategy 2

Fig. 16 Optimized control strategy

Compared with the above three control modes, although the control mode in Fig.16 (b) can achieve thermal uniformity of the secondary side devices, but from the simplicity of digital control implementation, Fig.16 (a) is the simplest and does not require complex logic processing. Therefore, this strategy is finally selected in this paper.

3.5 High-frequency Transformer Design

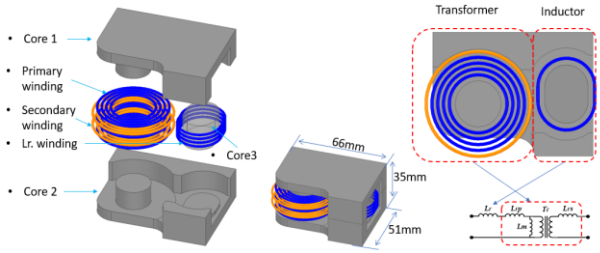

Fig. 17 High frequency transformer

The design of 500Khz transformer based on GaN devices is shown in Fig. 17. Which size is 66mm*51mm*35mm. The transformer and resonant inductor are designed independently and then physically integrated. The winding of the transformer should be exposed as far as possible to meet heat dissipation requirements. Compared with the traditional 120khz transformer design (Fig. 18), the 500khz high frequency transformer volume is reduced by 68%.

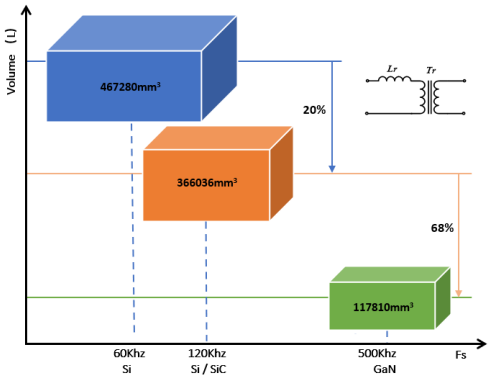

Fig. 18 Transformer volume comparison

4 Characters of GaN Devices

4.1 Why GaN Integrate Drivers

WBG power devices are capable of extremely high switching speeds, therefore monolithically integrating the driver stage and power stage is key to achieve highest switching frequencies, whilst keeping the signal clean, and eliminating any unwanted noise to influence the control and reliability of the device.

Navitas GaN-Fast power ICs are easy-to-use, high-speed, high-performance ‘digital-in, power-out’ building blocks. Monolithic integration of gate drive with the power stage enables virtually zero

loss in turn-off because the gate drive loop has essentially zero impedance. This also eliminates parasitic gate loop inductance and prevents gate ringing and glitching.

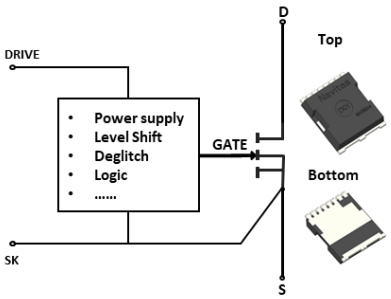

Fig. 19 Control block of NV651X series

In this paper, NV651X series produced by Navitas Semiconductor is selected for design. The internal control block diagram of the Toll-packaging integrated GaN device is shown in Fig. 19. It has the functions of Level Shift, deglitch and logic control to improve the reliability of its application.

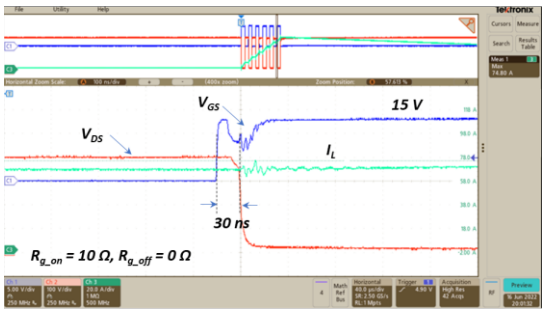

Fig. 20 Typical double pulse test waveform

Fig. 20 shows the typical test waveform based on double pulses. When the turn-off current is 70A, the waveform is still clean. The turn-on delay about 30ns can effectively prevent the bridge arm straight-through problem caused by external crosstalk.

4.2 Thermal solution

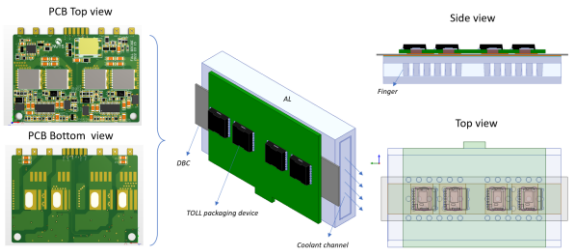

Fig. 21 Thermal solution for Toll-packaging

The full-bridge power board is developed using NV6514. GaN device adopts the heat dissipation treatment method of PCB Copper inlaid and DBC to control the thermal resistance of the system to the minimum (0.16℃/W), which is an effective heat dissipation treatment method as shown in Fig. 21. Simulation and experimental results verify the reliability of the proposed scheme.

5 Prototype and Test Results

A prototype of 6.6kW OBC+3.0kW Lv-DC/DC was designed based on GaN devices. The dimensions of the machine are shown in Fig. 22. The size is 210mm(L)∗192mm(W)∗61mm(H), the volume is about 2.5L, and the power density is up to 3.9Kw/L.

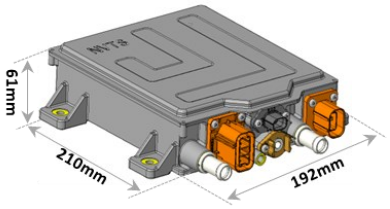

Fig. 22 Prototype size

5.1 Main Parameters

The main design parameters of the “2-in-1” bidirectional OBCM are shown in Table 2. The high-voltage battery range is 250V~ 500V, and the full power output of 280V~460V is supported. The low-voltage battery ranges is 9V~16V. The switching frequency of CCM PFC is 100khz; The bidirectional Boost-SRC resonant frequency is 400khz, the full load switching frequency range is 450~800Khz, and the maximum switching frequency is 1.2Mhz; The LVDC switching frequency is 60Khz. The charging power of the OBC is 6.6kW and the discharge power of 220V is 6.0KVA. LVDC has 3.0kW continuous output power and 3.6kW peak power.

	6.6kW Bi-OBC + 3.0kW LV DC/DC	
	Parameters	***Value***
OBC	Vac	85~265V
	Vbat range	250~500V，280~460Vfor full load
	Iac_Max	32A
	IHVo_Max	23.5A
	Power	6.6kW for charging and 220Vac/6.0KVA for discharging
	LPFC	50uH
	f_PFC	100Khz
	Resoanter inductor	4.0uH
	Resonant cap.	40nF (Equivalent)

	6.6kW Bi-OBC + 3.0kW LV DC/DC	
	Parameters	***Value***
	Resonant frequency	400khz
	Trans. turns ratio	1.2
LV-DC/DC	LV voltage rang	9~16v (Normal=13.5V)
	LV output Power	3.0Kw (3.6kw Peak)
	ILVo_Max	222A
GaN-Devices	Q1~Q4, S1~S8	NV6514
	S9~S12	NV6513

Table 2 Main parameters of "2-in-1" OBCM

5.2 Key Waveforms and Efficiency

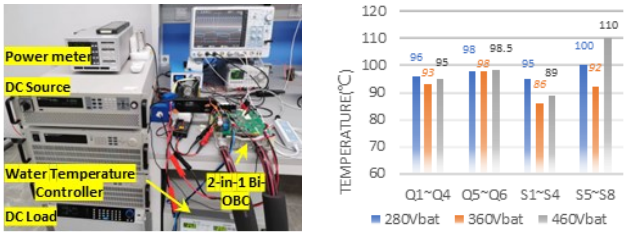

Fig. 23 Platform setup and devices thermal

The prototype test platform and devices thermal results are shown in Fig. 23. At the water temperature of 65°C and based on the heat dissipation method described in this paper, the temperature test results of GaN in 6.6kW charging mode output are show lower than 120 °C， which meet the worst-case application.

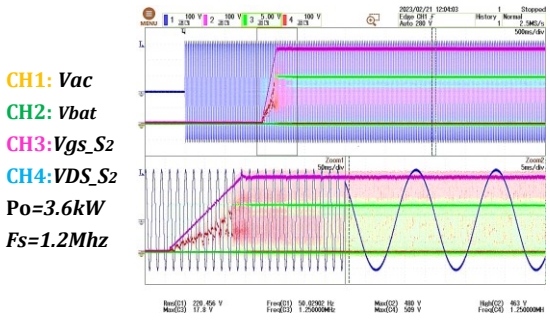

Fig. 24 Soft start waveform at 460Vbat

Fig. 24 shows the half-load soft starting waveform of the OBC at 460V output. Due to the characteristics of high output gain of Boost-SRC, the switching frequency has reached the preset upper limit of 1.2Mhz, which works in burst mode.

Fig. 25 is the waveform of 6.6kW steady-state operation with full load. CH2 is Vds of PFC and fs is 100Khz. CH3 is the Vgs signal of Bi-DC/DC and switching frequency up to 806Khz.

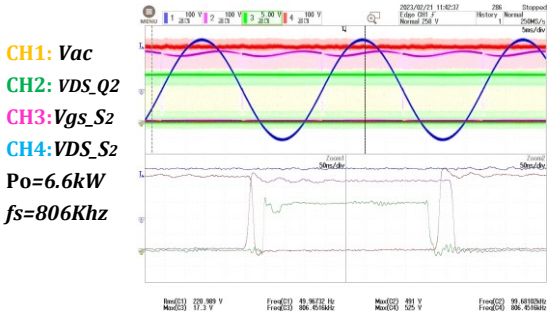

Fig. 25 Steady-state waveform at 460Vbat

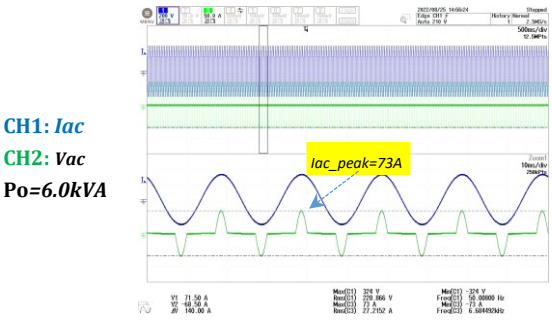

Fig. 26 Discharging 6.0KVA nonlinear load

The nonlinear load in discharge mode is not only an important specification to test the performance design of inverters, but also an important experiment to test the reliability of GaN devices operating under transient high current conditions. Fig. 26 shows the waveform of steady state operation under nonlinear load with output of 6.0KVA/220Vac. The peak AC current is as high as 73A. Due to the staggered parallel topology of the PFC stage, the average peak current of one single bridge arm is 36.5A, which is within the current tolerance range of NV6514.

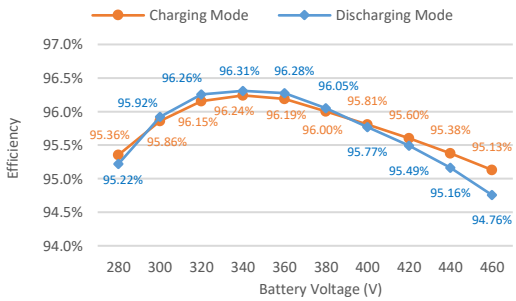

Fig. 27 Efficiency of charging and discharging

Under the condition of 45℃ water cooling, the efficiency curve of 6.6kw charging and 6.0kVA discharging is shown in Fig. 27. In charging mode, the efficiency is greater than 95% in the full range of 280V~460V output, and the peak efficiency is 96.24%. In discharge mode, the peak efficiency is

96.31%, and in the range of 400V~460V battery voltage range, the efficiency decreases rapidly mainly because the bidirectional DC/DC is in the state of high-frequency modulation, and the reactive power loss and turn-off loss are large. In the future, the method of varying Bus voltage can be used to optimize the efficiency.

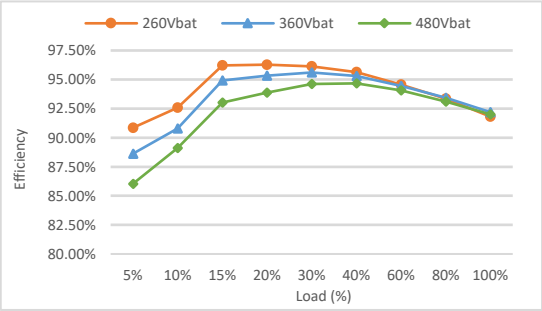

Fig. 28 Efficiency of HV-LV DC/DC

As part of the design of "2-in-1" OBC, 3.0kW LV-DC/DC adopts a hard-switched full-bridge solution. This technology is relatively mature, and correlation analysis is omitted. Only its efficiency curve at 13.5V output voltage is given as shown in Fig. 28. Although GaN devices are used on its high voltage side, there is almost no difference in switching loss and efficiency compared with traditional Si MOS because the switching frequency is only 60khz.

6 Conclusions

The "2-in-1" OBCM based on GaN device design adopts soft-switching, wide-gain resonant Boost-SRC topology. By taking advantage of the fast switching characteristics of GaN devices, the volume of the magnetic element is significantly reduced by increasing the switching frequency, thus achieving high frequency, high efficiency and high power density design. At the same time, the prototype verifies the feasibility and reliability of GaN devices application in high power conversion system.

7 Acknowledgment

The authors would like to thank Engineer from the Navitas Semiconductor Shanghai EV Design Center：Yunqi Chen，Jianbo Wei，Sicheng Gong，Zhongliang Xu, Dr. Xu and Zhen Zhou for their assistance in constructing and programming the experimental converter.

Reference

[1] Kim Y S, Oh C Y, Sung W Y, et al. Topology and Control Scheme of OBC–LDC Integrated Power Unit for Electric Vehicles[J]. IEEE Transactions on Power Electronics, 2016:1731-1743.

[2] Kumar, Misha, et al. Isolated Three-Port Bidirectional DC-DC Converter for Electric Vehicle Applications. In: 2022 IEEE Applied Power Electronics Conference and Exposition (APEC). IEEE, 2022. p. 2000-2007.

[3] Nussbaumer T, Raggl K, Kolar J W. Design guidelines for interleaved single-phase boost PFC circuits[J]. IEEE Transactions on Industrial Electronics, 2009, 56(7): 2559-2573..

[4] Zhao B, Song Q, Liu W, et al. Overview of Dual-Active-Bridge Isolated Bidirectional DC–DC Converter for High-Frequency-Link Power-Conversion System[J]. IEEE Transactions on Power Electronics, 2014, 29(8):4091-4106.

[5] Li B, Li Q, Lee F C, et al. A High-Efficiency High-Density Wide-Bandgap Device-Based Bidirectional On-Board Charger[J]. IEEE Journal of Emerging and Selected Topics in Power Electronics, 2018.

[6] Ammar A M, Ali K, Rogers D J. A Bidirectional GaN-Based CLLC Converter for Plug-In Electric Vehicles On-Board Chargers[C]//Conference of the Industrial Electronics Society. IEEE, 2020.

[7] SHAHED, Md Tanvir; RASHID, ABM Harun-Ur. Wide Bandgap Semiconductor Based High Performance Bidirectional Resonant Converter for Electric Vehicle Application. In: 2022 International Conference on Advancement in Electrical and Electronic Engineering (ICAEEE). IEEE, 2022. p. 1-6.

[8] Liu G, Jang Y, Jovanovic M, et al. Implementation of a 3.3-kW DC–DC Converter for EV On-Board Charger Employing the Series-Resonant Converter with Reduced-Frequency-Range Control[J]. IEEE Transactions on Power Electronics, 2017, 32(6):1-1.

[9] Minli J, Hao S. GaN-based High Frequency 6.6 kW Bi-directional DC/DC Converter for OBC Application[C]//2022 IEEE International Power Electronics and Application Conference and Exposition (PEAC). IEEE, 2022: 1330-1335.

[10] Li S, Lu S, Mi C C. Revolution of Electric Vehicle Charging Technologies Accelerated by Wide Bandgap Devices[J]. Proceedings of the IEEE, 2021, PP (99):1-19.

[11] Chen K J, Hberlen O, Lidow A, et al. GaN-on-Si Power Technology: Devices and Applications[J]. IEEE Transactions on Electron Devices, 2017, 64(3):779-795.

[12] https://911electronic.com/de/wide-bandgap-devices-will-enable-a-new-era-of-power-systems